Model-based feasibility assessment and evaluation of prostate hyperthermia with a commercial MR-guided endorectal HIFU ablation array

Vasant A. Salgaonkar[a)]
Thermal Therapy Research Group, Radiation Oncology, University of California San Francisco, 1600 Divisadero Street, Suite H-1031, San Francisco, California 94143

Punit Prakash
Department of Electrical and Computer Engineering, Kansas State University, 2077 Rathbone Hall, Manhattan, Kansas 66506

Viola Rieke and Eugene Ozhinsky
Department of Radiology and Biomedical Imaging, University of California San Francisco, 505 Parnassus Avenue, San Francisco, California 94143

Juan Plata
Department of Radiology, Stanford University, 1201 Welch Road, Stanford, California 94305

John Kurhanewicz
Department of Radiology and Biomedical Imaging, University of California San Francisco, 505 Parnassus Avenue, San Francisco, California 94143

I-C. (Joe) Hsu and Chris J. Diederich
Thermal Therapy Research Group, Radiation Oncology, University of California San Francisco, 1600 Divisadero Street, Suite H-1031, San Francisco, California 94143

(Received 22 August 2013; revised 4 February 2014; accepted for publication 7 February 2014; published 26 February 2014)

Purpose: Feasibility of targeted and volumetric hyperthermia (40–45 °C) delivery to the prostate with a commercial MR-guided endorectal ultrasound phased array system, designed specifically for thermal ablation and approved for ablation trials (ExAblate 2100, Insightec Ltd.), was assessed through computer simulations and tissue-equivalent phantom experiments with the intention of fast clinical translation for targeted hyperthermia in conjunction with radiotherapy and chemotherapy.
Methods: The simulations included a 3D finite element method based biothermal model, and acoustic field calculations for the ExAblate ERUS phased array (2.3 MHz, 2.3 × 4.0 cm^2, ∼1000 channels) using the rectangular radiator method. Array beamforming strategies were investigated to deliver protracted, continuous-wave hyperthermia to focal prostate cancer targets identified from representative patient cases. Constraints on power densities, sonication durations and switching speeds imposed by ExAblate hardware and software were incorporated in the models. Preliminary experiments included beamformed sonications in tissue mimicking phantoms under MR temperature monitoring at 3 T (GE Discovery MR750W).
Results: Acoustic intensities considered during simulation were limited to ensure mild hyperthermia ($T_{max} < 45$ °C) and fail-safe operation of the ExAblate array (spatial and time averaged acoustic intensity $I_{SATA} < 3.4$ W/cm^2). Tissue volumes with therapeutic temperature levels (T > 41 °C) were estimated. Numerical simulations indicated that T > 41 °C was calculated in 13–23 cm^3 volumes for sonications with planar or diverging beam patterns at 0.9–1.2 W/cm^2, in 4.5–5.8 cm^3 volumes for simultaneous multipoint focus beam patterns at ∼0.7 W/cm^2, and in ∼6.0 cm^3 for curvilinear (cylindrical) beam patterns at 0.75 W/cm^2. Focused heating patterns may be practical for treating focal disease in a single posterior quadrant of the prostate and diffused heating patterns may be useful for heating quadrants, hemigland volumes or even bilateral targets. Treatable volumes may be limited by pubic bone heating. Therapeutic temperatures were estimated for a range of physiological parameters, sonication duty cycles and rectal cooling. Hyperthermia specific phasing patterns were implemented on the ExAblate prostate array and continuous-wave sonications (∼0.88 W/cm^2, 15 min) were performed in tissue-mimicking material with real-time MR-based temperature imaging (PRFS imaging at 3.0 T). Shapes of heating patterns observed during experiments were consistent with simulations.
Conclusions: The ExAblate 2100, designed specifically for thermal ablation, can be controlled for delivering continuous hyperthermia in prostate while working within operational constraints. © *2014 American Association of Physicists in Medicine*. [http://dx.doi.org/10.1118/1.4866226]

Key words: hyperthermia, MR-guided HIFU, endorectal ultrasound, phased array, beamforming, modeling, simulation

1. INTRODUCTION

Hyperthermia has been combined successfully with several cancer treatment modalities, such as radiation therapy, chemotherapy, and hormonal therapy, and is known to improve treatment outcomes.[1–6] Mild hyperthermia (40–45 °C) can induce direct cytotoxicity in tumors, radiosensitize cancer cells by impairing DNA repair mechanisms, and enhance blood flow in tumor microenvironments to increase tumor oxygenation and facilitate drug delivery.[7] It may also be used to enhance localized drug delivery[8] and gene therapy[9] as reported in some recent investigations. Hyperthermia treatment can be administered by applicators that deliver radiofrequency energy, microwaves, or ultrasound energy.[10–12] These devices may be designed for extracorporeal placement, intracavitary or endoluminal deployment, or interstitial or percutaneous insertion.[13–15] Typically, these treatments involve heating tumor targets for 30–60 min duration. For maximum clinical benefit, uniform temperature profiles are desired within target volumes, with minimum temperature greater than 40 °C and 6–10 min cumulative thermal dose at 43 °C.[16–18] Administering hyperthermia to tumors situated deep inside the body presents significant clinical challenges such as selective energy deposition within the tumor while thermally sparing surrounding structures, and sufficient thermometry for reliable treatment monitoring.[19,20] Such difficulties may be encountered during hyperthermia delivery to focal cancer targets in prostate and other organs inside the pelvic cavity.

Endorectal ultrasound (ERUS) transducer arrays have been investigated for hyperthermia delivery to the prostate and studies devoted to design and preclinical evaluation of such devices have been reported.[21–26] Clinical studies have demonstrated feasibility of safe, reliable, and effective application of prostate hyperthermia with ERUS applicators.[27–30] Currently, MR guided high intensity focused ultrasound (MRgHIFU) systems are being increasingly utilized for noninvasive or minimally invasive thermal ablation of soft tissue tumors in multiple organ sites.[31,32] Typically, these are multielement phased array applicators capable of delivering ultrasound energy with precise spatial control. Integration with MRI and MR thermometry has enabled real-time guidance and monitoring of HIFU ablation procedures.[33] Endorectal ultrasound applicators, consisting of phased arrays or multi-sectored devices, have been investigated for delivering hyperthermia under MR guidance and control.[25,26,34]

Recent studies have utilized MR-guided HIFU systems for enhancement of drug delivery in cancer treatment. This has been achieved through pulsed mode operation of the HIFU system,[35–37] rapid mechanical,[38] or electronic translation[39] of the HIFU focus, or simultaneous multipoint focusing of HIFU phased array[34] to heat small volumes. Enhancement in uptake of free-flowing[35–37] and liposome-encapsulated drug has been achieved.[38–40]

ExAblate 2100 (InSightec Ltd., Haifa, Israel) is a commercially available MR-guided thermal ablation system. Several different ultrasound transducer modules are provided with this system. They are designed for treating various disease sites. One such transducer module is an ERUS phased array designed for prostate ablation [Fig. 1(a)]. Treatments are planned using detailed anatomical MR images that facilitate identification of target zones, and help in ERUS array placement and orientation. Based on real time MR temperature imaging (MRTI), the ERUS array can be utilized to translate (mechanical or electronic scanning) a small HIFU focal pattern in 3D and perform repetitive ablations to coagulate overlapping lesions that cumulatively cover the entire target volume.[41,42] In contrast to HIFU, hyperthermia requires more diffused energy deposition sustained over longer durations to establish uniform temperature distribution and sufficient thermal dose within the entire targeted volume.

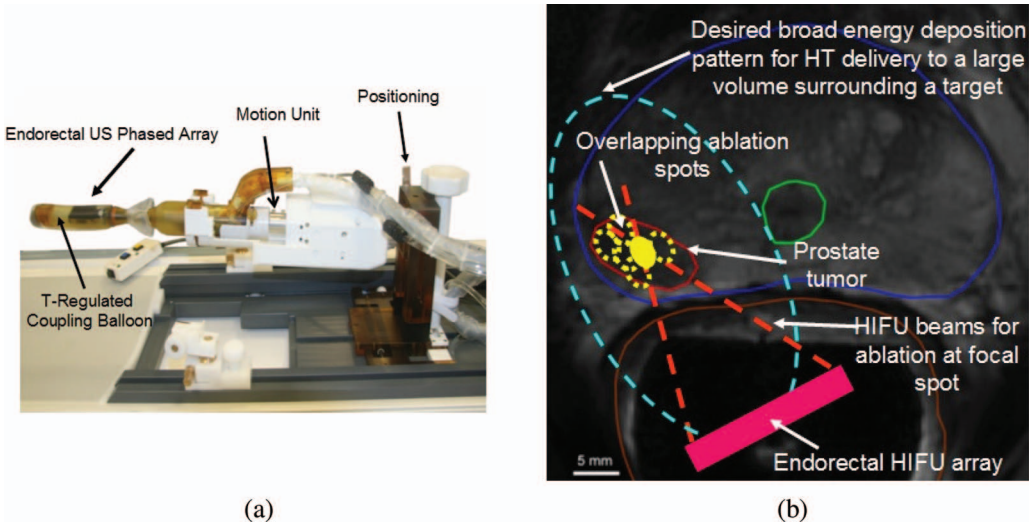

FIG. 1. (a) MR-compatible ExAblate 2100 endorectal ultrasound phased array (2.3 MHz) ablation system. (b) Illustration showing differences in sonications patterns required for ablation and mild hyperthermia in the prostate to treat focal cancer lesions. The axial MR scan belongs to the representative patient case number 1 utilized during patient specific models presented in this paper.

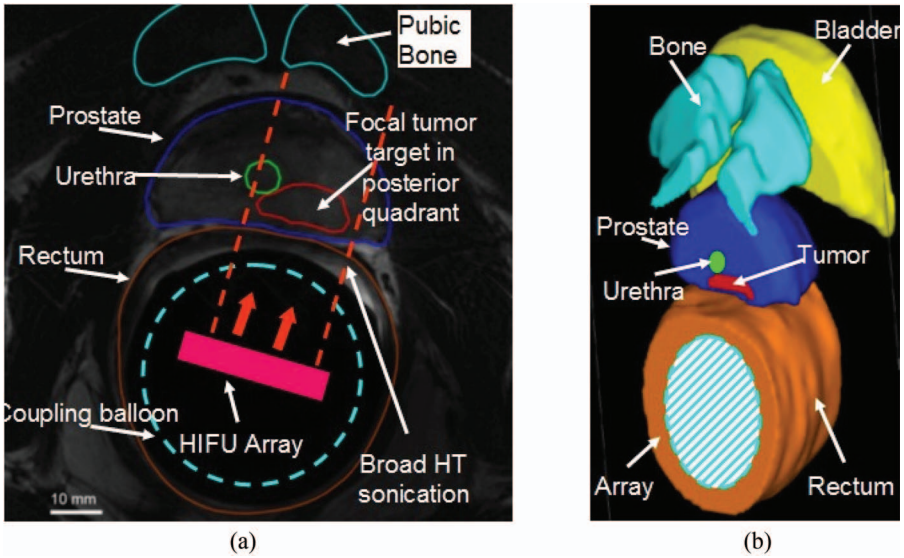

FIG. 2. (a) Axial MRI scan where the tumor target inside the prostate identified and segmented along with other critical anatomical structures. It belongs to the representative patient case number 2 utilized during patient specific models presented in this paper. (b) 3D model geometry created from serial axial scans following segmentation of organs.

Array beamforming and phasing requirements of these sonications are very different from conventional HIFU exposures [Figs. 1(b) and 2(a)]. Hence, in this study, the feasibility of protracted hyperthermia to prostate targets (focal targets, posterior quadrants, and hemigland) with the ExAblate 2100 array was assessed through simulations, modeling, and preliminary experiments. Operational modifications required for continuous wave (CW) sonications, unlike previous studies where pulsed-HIFU was utilized to maintain hyperthermic temperatures,[35–37] and continuous volumetric multiplane MRTI was identified within system hardware and software constraints.

The ExAblate 2100 system is already in clinical trials for prostate ablation.[41–43] If it can be successfully adapted for protracted hyperthermia, it can be potentially fast-tracked for clinical application. With this motivation, this initial study employed theoretical and experimental techniques to identify operational modifications, and assess the feasibility and capability of safe and reliable MR-guided prostate hyperthermia with the ExAblate 2100 prostate applicator.

2. METHODS

In this study we utilized computer simulations and thermal dosimetry experiments to assess the feasibility of prostate hyperthermia with the ExAblate 2100 MR-guided endorectal ultrasound (MRgERUS) phased array. The simulation studies consisted of acoustic pressure calculations and array beamforming for generating hyperthermia-specific US energy deposition patterns. Biothermal models were employed to ascertain US-induced heating for the various sonication strategies considered. Clinical images were used to generate anatomical geometries and finite element method (FEM) meshes for representative patient datasets. The initial experiments were employed to demonstrate implementation of hyperthermia-specific sonication strategies on the ExAblate phased array ablation system.

2.A. Acoustic power deposition calculations

Acoustic calculations were performed for the ExAblate 2100 prostate phased array. To ensure realistic modeling, all array design specifications and details provided by Insightec Ltd. were incorporated. This included operating frequency (2.3 MHz), array dimensions (23×40 mm^2), independent power channels ($\sim$1000), individual rectangular element size, proprietary element layout, and electrical connection scheme which includes clustering of distributed elements to have same phasing, phase encoding and round-offs, sonication intensities and sonication duration limitations, duty cycles, and software constraints.

The acoustic pressure field from an individual array element was computed using the rectangular radiator method developed by Ochletree and Frizzel.[44] Considering each element as a simple rectangle-shaped baffled piston source, the cumulative acoustic pressure (p_0) generated in a lossless aqueous medium because of continuous wave excitation of N elements can be calculated using the following equation:

$$p_0(x, y, z) = \frac{j\rho c \Delta A}{\lambda} \sum_1^N \frac{u_n}{R} e^{-jkR} \times \sin c\left[\frac{k(x-x_n)\Delta w}{2R}\right] \sin c\left[\frac{k(y-y_n)\Delta h}{2R}\right]. \quad (1)$$

In Eq. (1), the phased array transducer is assumed to be in plane $z = 0$, ρ is the density, c is the speed of sound, λ is the wavelength, k is the wave-number, $u_n = |u_n| \times \exp(-j\varphi_n)$ is the complex particle velocity at the surface of the nth element and φ_n is the phase angle, Δw, Δh, and ΔA are the width, height and surface area of an element, respectively, x_n and y_n are the centers of the nth element, and $R = [(x - x_n)^2 + (y - y_n)^2 + z^2]^{0.5}$. The accuracy of the sinc function approximation in Eq. (1) is dictated by the expression $\Delta w \leq (4\lambda z/F)^{0.5}$. The calculations discussed above are based on Ref. 44. F refers to the distance between the ultrasound source and a spatial point in the field, relative to the distance of nearfield-farfield transition when the source size is Δw.[44] A larger value of F implies greater accuracy in pressure estimation at a given distance of z but it also requires smaller source size (Δw) and increases the number of computations. For the dimensions of the square array elements and the operating frequency for the array considered in this simulation study, F always exceeded 151 for a distance greater than 15 mm (approximate coupling balloon radius for the prostate array beyond which acoustic heating occurs). An increase in F values did not yield substantial changes in the acoustic intensity calculations.

The acoustic energy (Q_{ac}) deposited at a point in the simulation space is given in Eq. (2).

$$Q_{ac}(x, y, z) = 2 \propto (x, y, z) \frac{|p_0(x, y, z)|^2}{2\rho c} \times \exp\left[-2z \int_0^z \mu(z) \cdot dz\right]. \quad (2)$$

In Eq. (2), $|p_0|$ is peak pressure amplitude, α is acoustic absorption, μ is acoustic attenuation, ρ is density, and c is sound speed. An averaged acoustic attenuation was applied along the ultrasonic beam path. All scattered energy was assumed to be absorbed locally. 60% transmission of longitudinal acoustic waves was assumed at the bone-tissue interface (more details in patient specific modeling that follows later) with reflection, refraction, and shear wave conversion being neglected.[45] Only linear propagation of acoustic energy was modeled. Modeling constants related to acoustic properties of tissues have been compiled in Table I.

TABLE I. Constants used in biothermal and acoustic models are tabulated here. These values have been obtained from Refs. 45, 54, 70, and 71. Physical and physiological properties of tissue were assumed to be homogeneous in generalized models, and varied with tissue type in patient-specific models.

Parameter	Units	Value
k (thermal conductivity)	W/m/°C	0.56
		0.5 (phantom)
		0.5 – 8.0 (range used in generalized model)
		1 (bone)
ω_b (blood perfusion)	kg/m^3/s	2.5 (prostate)
		5 (periprostatic tissue)
		4 (rectum)
		0 (phantom)
C_b (specific heat of blood)	J/kg/°C	3720
C (specific heat of tissue)	J/kg/°C	3600
		3500 (phantom)
T_b (body/blood temperature)	°C	37
c (sound speed)	m/s	1500
ρ (density)	Kg/m^3	1060
f_0 (center frequency)	MHz	2.3
		5.3 (generalized model)
		5.3 (prostate)
α (acoustic absorption)	Np/m/MHz	6 (rectum)
μ (acoustic attenuation)		5 (periprostatic tissue)
		250 (bone)
		5.8 (phantom)

2.B. Array beamforming

To modify energy deposition patterns, ERUS elements were excited with specific phase delay values. As allowed by the ExAblate system, all elements could be excited using uniform acoustic intensity magnitude only. The value of acoustic intensity depended upon the input power to the entire array. The phase values were computed based on element position and focusing characteristics required to generate the requisite beam patterns. Calculations of phase values did not take into account tissue attenuation. They employed estimates of phase angle using the difference in Cartesian distance between the center of an array element and focusing position.[22,46] Differences in path length as a fraction of wavelength were determined, and the corresponding phase delay was calculated such that a distance of $\lambda/2$ equals $\pm 180°$. These calculated phase delays were rounded off to match the digital resolution of the phase shifting hardware (proprietary information) of InSightec ExAblate system. Attenuation was considered during ultrasound power deposition calculations [Eq. (2)]. Phasing schemes investigated in this study are described next. In this description, azimuth (AZ) refers to dimension along array length (40 mm), elevation (EL) refers to the dimension along array width (23 mm), range (RN) or depth refers to orthogonal distance from the array surface. As described in Subsection 2.A, complex phase refers to $\Phi = \exp(-j\varphi)$ where φ is called phase angle.

2.B.1. Multipoint focusing

This sonication scheme was explored to selectively heat small targets, such as localized focal cancer targets located in the posterior peripheral zone of the prostate (10–15 mm wide, 1–2 cm^3 volume). It consisted of beamforming techniques which simultaneously focused the ERUS array at multiple (4–8) points [Fig. 3(a)]. Placement of the foci was identified through an iterative and empirical procedure based on the representative clinical cases. Representative patient exam-

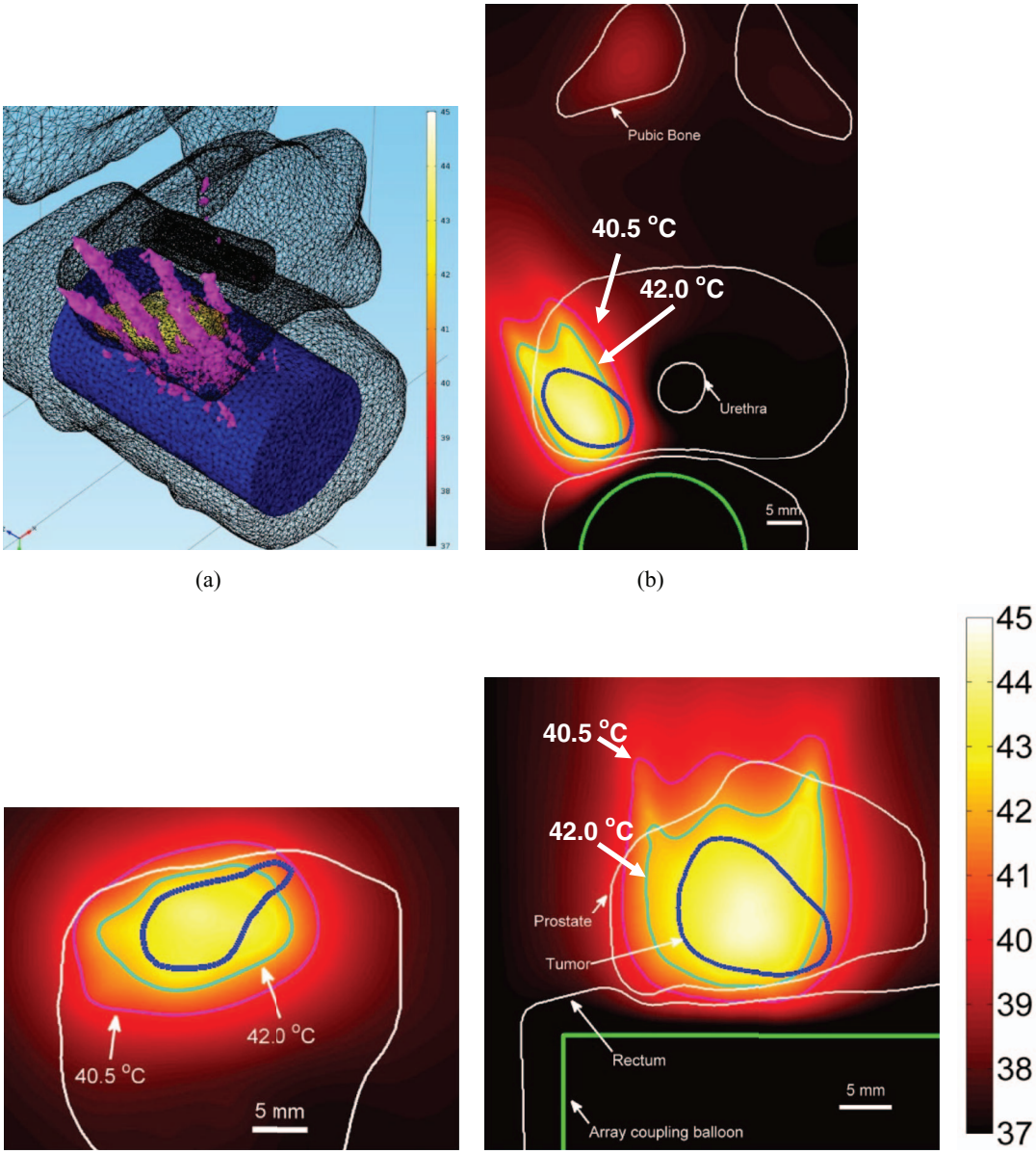

FIG. 3. Conformable hyperthermia to a small focal region in the right quadrant of the prostate containing cancerous tissue. (a) Multifocal pattern (six simultaneous foci) employed in hyperthermia delivery (plotted SAR contour = 300 W/kg) is overlaid upon 3D anatomical geometry along with temperature on tumor surface. Temperature distribution plotted in (b) axial, (c) coronal, and (d) sagittal planes through target center (I = 0.75 W/cm^2, $T_{max} = 44.5\,^{\circ}$C).

ples are discussed in greater detail in Subsection 2.C. Multipoint focusing was considered for cancer targets located at a distance of 10–20 mm from the rectal wall and 25–35 mm from the ERUS array (accounting for ∼15 mm radius of the cooling balloon). The sonication configurations considered here had focus points placed ∼35 mm deep and 5–10 mm transverse distance from the array axis. Optimization of focus positions was beyond the scope of this study. It has been investigated for multipoint focusing in Ref. 47. Here, phase values were first computed for all transducer elements in order to focus the array at each individual focusing point as shown next.

$$\varphi_{mn=k} \cdot (|\boldsymbol{R}_{mn}| - |\boldsymbol{R}_n|). \tag{3}$$

In Eq. (3), φ_{mn} is the phase angle for the mth transducer element and the nth focal point, $|\boldsymbol{R}_{mn}|$ is the distance between mth transducer element and nth focal point, and $|\boldsymbol{R}_n|$ is the distance between the nth focal point and center of the transducer. The complex phase applied to each transducer channel in order to obtain simultaneous multipoint focusing was

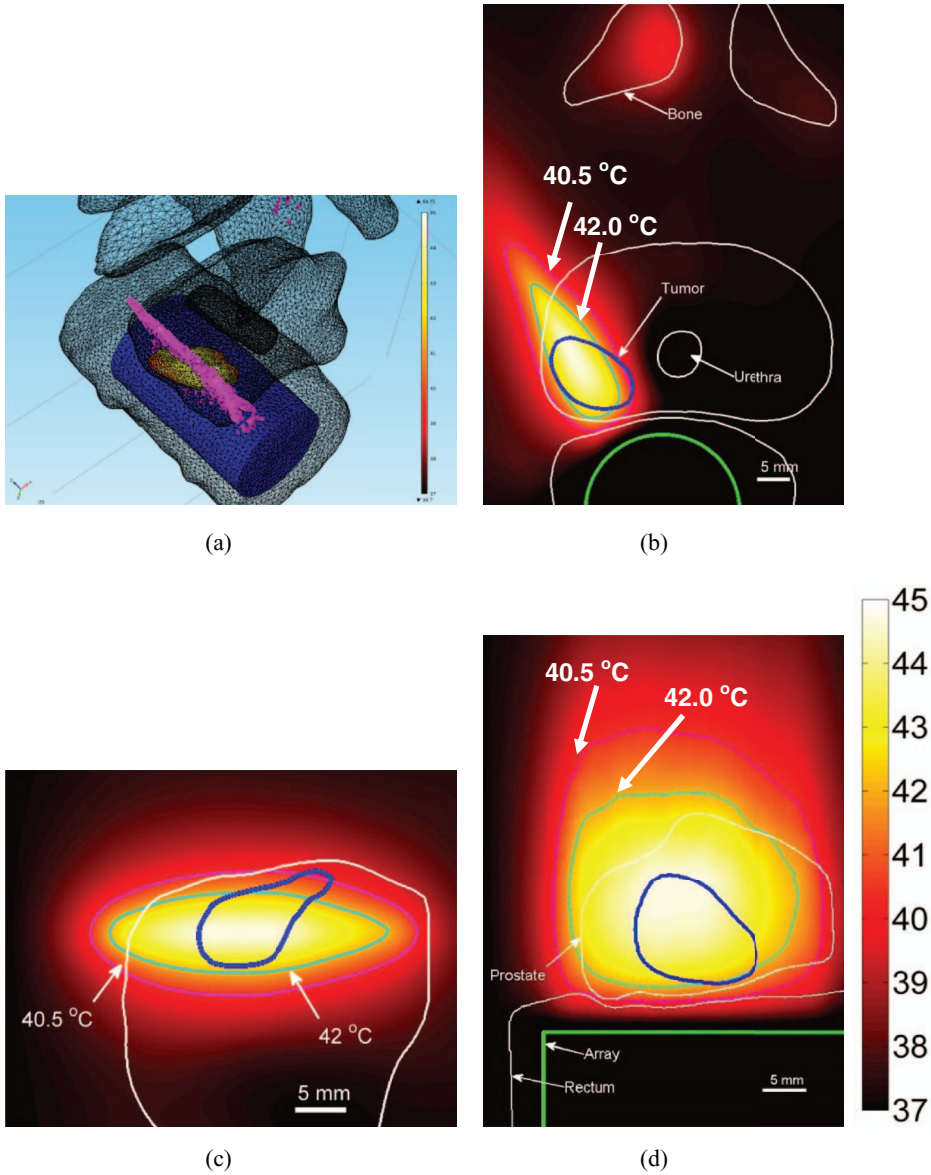

FIG. 4. Hyperthermia to a small focal cancer target region in right quadrant of the prostate using curvilinear focusing. (a) Curvilinear focusing (35 mm depth) pattern (plotted SAR contour = 300 W/kg) is overlaid upon 3D anatomical geometry, along with temperature on tumor surface. Temperature distribution plotted in (b) axial, (c) coronal, and (d) sagittal planes through tumor center (I = 0.75 W/cm^2, T_{max} = 44.7 °C).

computed using the equation shown next.

$$\Phi_m = 1/N \cdot \sum_{n=1}^{N} e^{(-j\varphi_{mn})}. \tag{4}$$

In Eq. (4), N is the total number of simultaneous foci and $j = \sqrt{(-1)}$. Φ_m is a complex phasor. Angle(Φ_m) is the phase angle applied to the mth transducer channel.

2.B.2. Cylindrical or curvilinear focusing

To simulate focusing behavior of a curvilinear or cylindrically focused transducer, the ERUS array was focused along the array elevation direction [Fig. 4(a)]. Phase delays were computed based only on the distance between ERUS elements and a cylindrical focus axis (based only on the focusing depth and element elevation). This sonication pattern was explored to deliver heat to small targets in the posterior prostate, similar to the targets where multipoint focusing was considered. Again, positioning of the focus was performed using iterative and empirical methods. Here the focusing depth was set between 25 and 35 mm for delivering zonal hyperthermia (10–15 mm wide targets) along the prostate length. Complex phase computation is shown next.

$$\Phi_m = \exp\left[-jk\left(\sqrt{EL_m{}^2 + RN_F{}^2} - RN_F\right)\right]. \tag{5}$$

In Eq. (5), Φ_m is complex phasor for the mth transducer element, RN_F is the focus position in the range dimension and EL_m is the transducer element position in the elevation

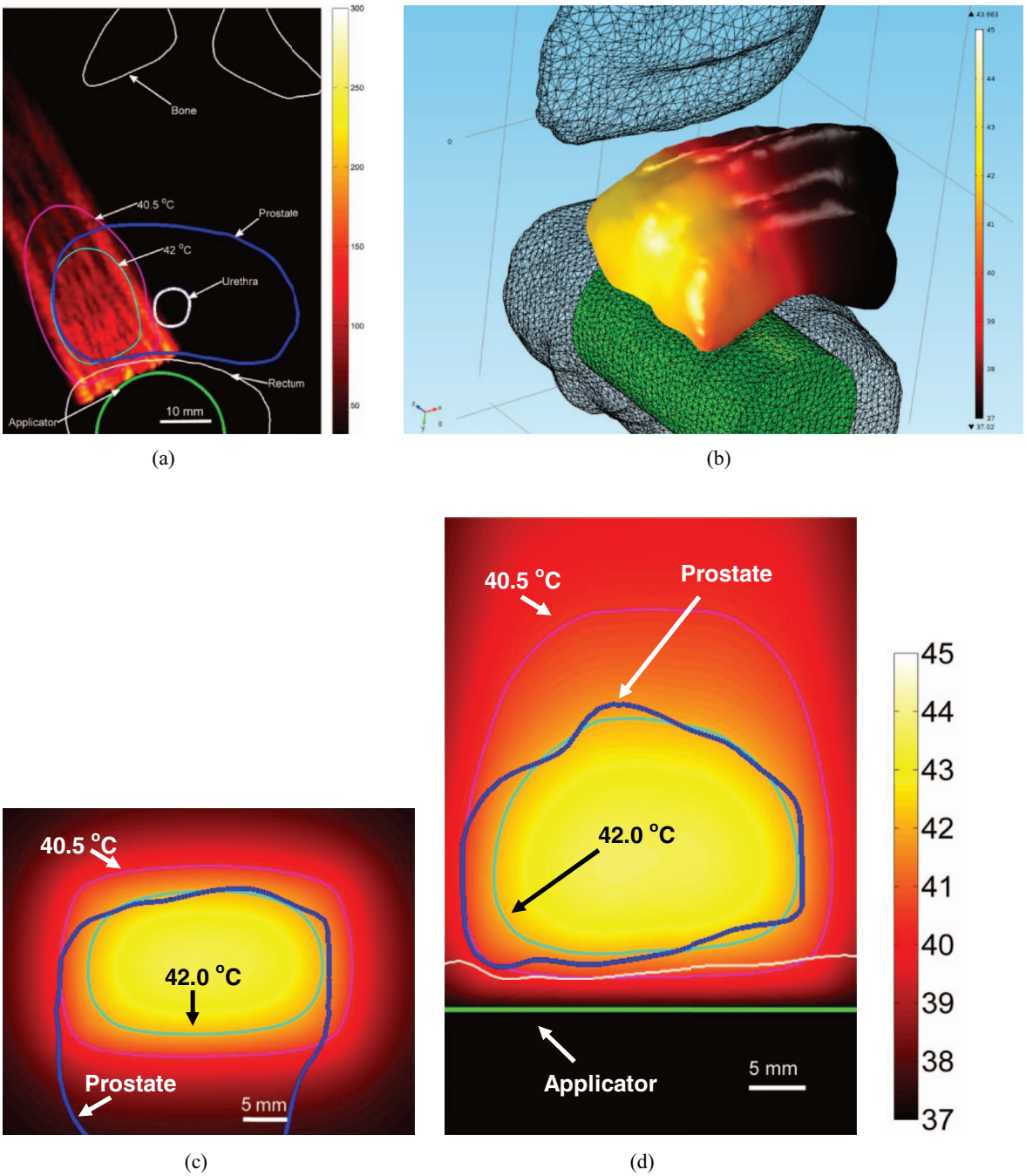

FIG. 5. (a) SAR distribution obtained by planar sonication is plotted in the central axial plane of a representative case. Temperature and anatomy overlay to show hemi-gland heating of the prostate is shown in (b) 3D, (c) coronal plane 30 mm from the applicator and (d) sagittal plane through the applicator. ($I = 0.9$ W/cm^2, $T_{max} = 43.7\,^{\circ}$C).

dimension and k is the wave-number. The transducer element is assumed to be at RN = 0, and the focus is assumed to be at EL = 0.

2.B.3. Planar sonications

Planar beam patterns were simulated by setting uniform complex phase ($\Phi_m = 0$) for all power channels [Fig. 5(a)]. This achieved the effect of synchronous operation of all ERUS array elements to mimic the functionality of a planar rectangular transducer with a large aperture.[48] These sonications were explored for hyperthermia to hemigland prostate or posterior quadrants of the gland.

2.B.4. Diverging sonications

This approach was explored to heat wide focal targets near the posterior periphery of the prostate or posterior

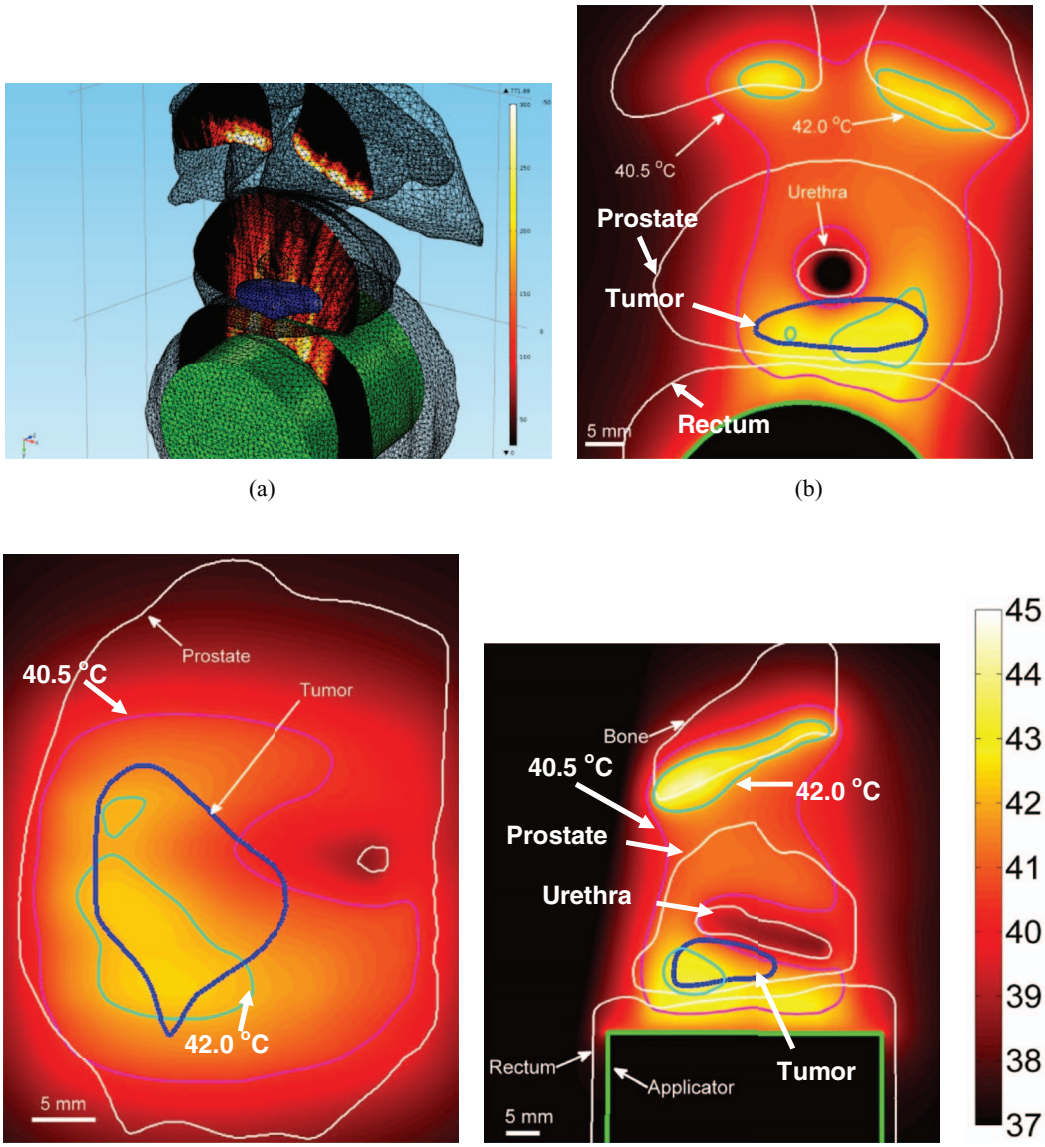

FIG. 6. (a) SAR distribution obtained by cylindrically diverging sonication is plotted in the central axial plane (b) Corresponding temperature distribution obtained in the same central axial plane is shown. Temperature distribution in an oblique sagittal slice (c) and an oblique coronal slice is also shown ($I = 1.35$ W/cm^2, $T_{max} = 44.8\,^{\circ}$C).

quadrant of the gland Fig. 6(a). Cylindrically diverging beam patterns were considered to heat such targets. Smith *et al.* explored endorectal phased arrays with cylindrical elements to generate diverging sonication patterns with 120° angular expanse.[26] Beamforming techniques were employed to generate similar diverging patterns with the ExAblate prostate array (which consists of rectangular elements). Phase delay beamforming was utilized to simulate cylindrical transducers with radii of curvature between 10 and 60 mm and an aperture of 2.3 cm width (phased array width). The range of curvature radii was identified for patient specific hyperthermia using empirical methods. Phase delays were again computed using only the radius of curvature value and elevation position of the array elements. The goal of this beamforming was to produce cylindrically diverging wave-fronts that may heat targets close to the array but wider than its elevation dimension (23 mm). Complex phase computation is shown next.

$$\Phi_m = \exp\left[jk\left(\sqrt{EL_m{}^2 + RC^2} - RC\right)\right]. \tag{6}$$

In Eq. (5), Φ_m is complex phasor for the mth transducer element, RC is the radius of curvature and EL_m is the transducer element position in the elevation dimension and k is the wave-number. The transducer element is assumed to be at RN = 0, and the focus is assumed to be at EL = 0.

2.C. Biothermal models

Heat transfer was modeled using the Pennes bioheat equation as shown below.[49]

$$\rho C_{pt}\frac{\partial T'}{\partial t} = \nabla \cdot [k_t \nabla T'] - \omega_b c_{pb} T' + Q_{ac}. \quad (7)$$

In Eq. (7), ρ is the density, c_{pt} and c_{pb} are specific heat capacity values for tissue and blood, respectively, k_t is thermal conductivity, T' is the temperature rise over basal/blood temperature, ω_b is the blood perfusion and Q_{ac} is the heat generated due to acoustic energy deposition. Modeling constants related to thermal properties of tissues have been compiled in Table I.

Biothermal models were employed to calculate temperature profiles with generalized and patient-specific geometries. For these models, the input power was computed through an iterative empirical process where the acoustic intensity was varied to obtain a maximum temperature estimate between 44.5 and 45.2 °C. This maximum temperature was employed because the goal of hyperthermia is to cause sub-lethal damage in the target tissue using heat energy alone. The input acoustic intensity was always restricted within operational limits of the ExAblate 2100 ERUS array. Through communications with InSightec it was established that acoustic outputs up to 3.4 W/cm^2 could be delivered safely. Dimensions of resulting simulated 40 and 41 °C temperature clouds were computed. These two temperature values were chosen because the therapeutic range of hyperthermia is between 40 and 45 °C (Ref. 10) and thermal radiosensitization is known to occur ~41 °C,[50,51] if delivered for 30–60 min. Also new formulations of temperature sensitive liposomes can be activated at 40 °C and be used for targeted drug delivery.[19]

Generalized models were also utilized to conduct parametric analyses. Changes in treatment parameters such as blood perfusion, phased array cooling, and phased array duty cycles were considered. The input acoustic intensity (or power) was varied to maintain maximum temperature close to 45 °C and maximize the heated target volume for a given combination of parameter values.

2.C.1. Model geometry

Generalized model geometry consisted of the ERUS phased array situated inside a 15-mm radius cylindrical balloon filled with degassed water sonicating homogenous soft tissue. For these models physiological parameters, such as blood perfusion, acoustic parameters, and thermal properties of soft tissue, were assumed to be homogeneous.

Patient specific model geometry was created from two representative patient data sets [example shown in Figs. 1(b) and 2(a)]. Critical organ structures such as the prostate and cancer target volume, bladder, rectum, urethra and pubic bones were manually segmented from serial MR axial images by using contouring tools available in a 3D modeling software (Mimics and 3-Matic, Materialise, Belgium). Both patients had focal prostatic tumor nodes in the posterior peripheral zone near the gland apex. The first patient had a unilateral target confined to the right side (prostate volume = 22 cm^3, tumor volume = 1.2 cm^3). The second patient had a bilateral target, but predominantly on the left (prostate volume = 19 cm^3, target volume = 1 cm^3). Due to the high acoustic absorption of bone and acoustic penetration depth at 2.3 MHz, acoustic energy may cause some heating in the pubic symphysis located anterior to the gland. To study the impact of bone heating on treatment quality, patient cases were selected with pubic bone located far (25–30 mm, case 1) or near the gland (8–10 mm, case 2). The ERUS phased array was assumed perfectly coupled to the rectal wall by a distensible cooling balloon that contained temperature-regulated circulating water for cooling of rectal tissue, and protection of the phased array. Position and orientation of the ERUS phased array was set to direct acoustic energy at the target volume. In a treatment scenario with the ExAblate ERUS array, such positioning would be achieved using translation and rotation module of the ExAblate system. Bladder was assumed to contain water and urethral cooling was applied as required.

2.C.2. Boundary conditions

For both generalized and patient-specific geometries, the outer simulation boundaries were assumed to have constant temperature, which was set to the same value as blood/basal temperature (37 °C). The ERUS cooling balloon and urethral cooling balloon were modeled to have constant temperature dictated by cooling water flow (T_{cool} = 22–41 °C). Several studies about hyperthermia to the prostate using endorectal ultrasound utilize a bolus of temperature-controlled water for applicator coupling and rectal wall protection.[21,22,27,29,30] The InSightec system can regulate bolus temperature over a large range (as low as 10 °C). Such temperatures may provide effective cooling but hyperthermia procedures may extend for 30–60 min and patients may experience some discomfort due to prolonged contact with a cooled ERUS probe, making higher water bolus temperatures necessary.

2.C.3. Numerical evaluation

The biothermal and acoustic models were evaluated using COMSOL Multiphysics 3.5a and 4.3 (Comsol Inc., Burlington, MA), a FEM software program, and Matlab 7.5 (MathWorks Inc., Natick, MA). Patient specific geometry was created from serial axial MRI scans. They were loaded into Mimics 15.01 (Materialise, Belgium) and critical anatomical structures were manually segmented (based on prior experience and supplementary information from the patient cases) using drawing tools available in this software. Mimics tools were also used to convert the segmented contours into 3D volumes following smoothing (smooth factor = 0.9, iterations = 9) and wrapping operations. Smooth 3D volumes of anatomical structures were generated with these steps. The FEM mesh parameters, in terms of mesh element dimensions, were selected through an iterative process to ensure a stable thermal solution. The mesh sizes were varied from 0.4 to 1.8 mm in the target region and interfaces such as bone and rectum. Convergence testing with smaller element sizes demonstrated sufficient accuracy. Patient specific models had ~550 000

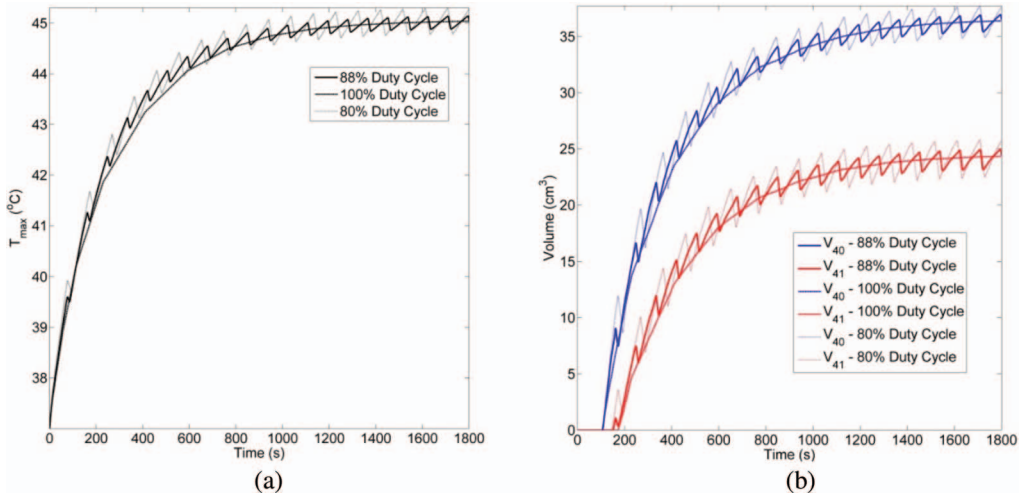

FIG. 7. Comparison of (a) T_{max} *vs* time, (b) V_{40}, V_{41} *vs* time for 80%, 88%, and 100% duty cycle for planar sonication in generalized model is shown here. Acoustic intensity was adjusted to maintain constant energy.

tethrahedral mesh elements with ~750 000 nodes. The smallest element size was ~0.4 mm situated inside the cancer target, the largest element was 7 mm at simulation space extremity where direct ultrasound heating did not occur, and the average element quality (aspect ratio of height and base of tetrahedra) was 0.44.

Steady state implementation of Eq. (3) was utilized during all patient-specific models. The generalized models employed steady state or transient version (Fig. 7) of Eq. (3). The generalized models were also used for a parametric study that investigated the impact of blood perfusion, applicator cooling and sonication duty cycle on heating performance of the array. Steady state models utilized "Direct (PARDISO)" and transient models utilized "Geometric Multigrid" implicit solver s in COMSOL Multiphysics, with convergence tolerance of 1×10^{-6}. All simulations were performed on a workstation with Intel Xeon CPU Dual core, 2.5 GHz, 16 GB RAM, and Windows Vista. Typical simulation time was 25–40 min for acoustic and biothermal calculations.

2.D. Evaluation in tissue phantom under MRTI

To demonstrate beamforming strategies developed in the simulation studies, some hyperthermia-specific sonications were implemented on ExAblate 2100 ERUS phased array ablation system. Phasing patterns, specific to the proprietary layout of the ERUS array, were applied to the phased array using research GUI and tools provided in the InSightec ablation system. This research version consists of utility interfaces (Control computer interface with software version 5.3.2) which allow the ablation system to be programmed with greater flexibility. Through these GUI packages, it is possible to set sonication parameters such as input power and exposure time, and also implement customized beamforming patterns on the system.

In the preliminary tests presented here, the ExAblate prostate array was employed to heat tissue-mimicking phantoms provided for quality assurance and calibration by InSightec (Model TXS-100, ATS Laboratories, Inc, Bridgeport, CT). The phantom was shaped like a lightly tapered cylinder ~10.2 cm in diameter and ~12.7 cm in height with acoustic attenuation = 0.503 dB/cm/MHz and sound speed = 1538 m/s.[52] Experiments were conducted in a 3 T MRI scanner (GE Healthcare Discovery MR750W) where imaging and temperature data was obtained by a birdcage head coil (GE). Complex MR images were acquired in multiple imaging planes for MRTI, with all slices in the same orientation. For the data presented here, image slices were either in axial or coronal orientation. Five axial planes were recorded with slice thickness of 5 mm, inter-slice spacing of 1.0 mm, and the center slice was positioned at the array center. Five coronal planes were recorded with slice thickness of 5 mm, inter-slice spacing of 0.5 mm, and the center slice was positioned at the 35 mm distance from array surface. MRTI was performed using a spoiled gradient echo sequence with the following imaging parameters: TE = 16 ms, BW = ±31.2 kHz. The FOV was 14 cm, slice thickness = 5 mm, flip angle = 30, and matrix size = 256 × 256 pixels. The complex images were transferred to a workstation in real-time and temperature images were reconstructed with the proton resonance frequency (PRF) method.[53]

For these initial experiments, conservative exposure parameters were employed. Electrical power was set at 10 W (time-averaged surface acoustic intensity ~0.88 W/cm^2). Throughout this paper acoustic intensity refers to time-averaged acoustic intensity computed at the surface of the phased array applicator (I_{SATA}). Uniform excitation magnitude was assumed across the entire phased array. For this power level, operational constraints of the ExAblate 2100 system only allowed sonication durations of 5 min. Three sets of such 5-min sonications were conducted to obtain a total heating time of 15 min. Time duration between consecutive sonications was 5–10 s. After a single sonication, the system required reinitialization and it resulted in this short time delay between consecutive sonications. To ensure safe operation and protection of the prostate array, cooling

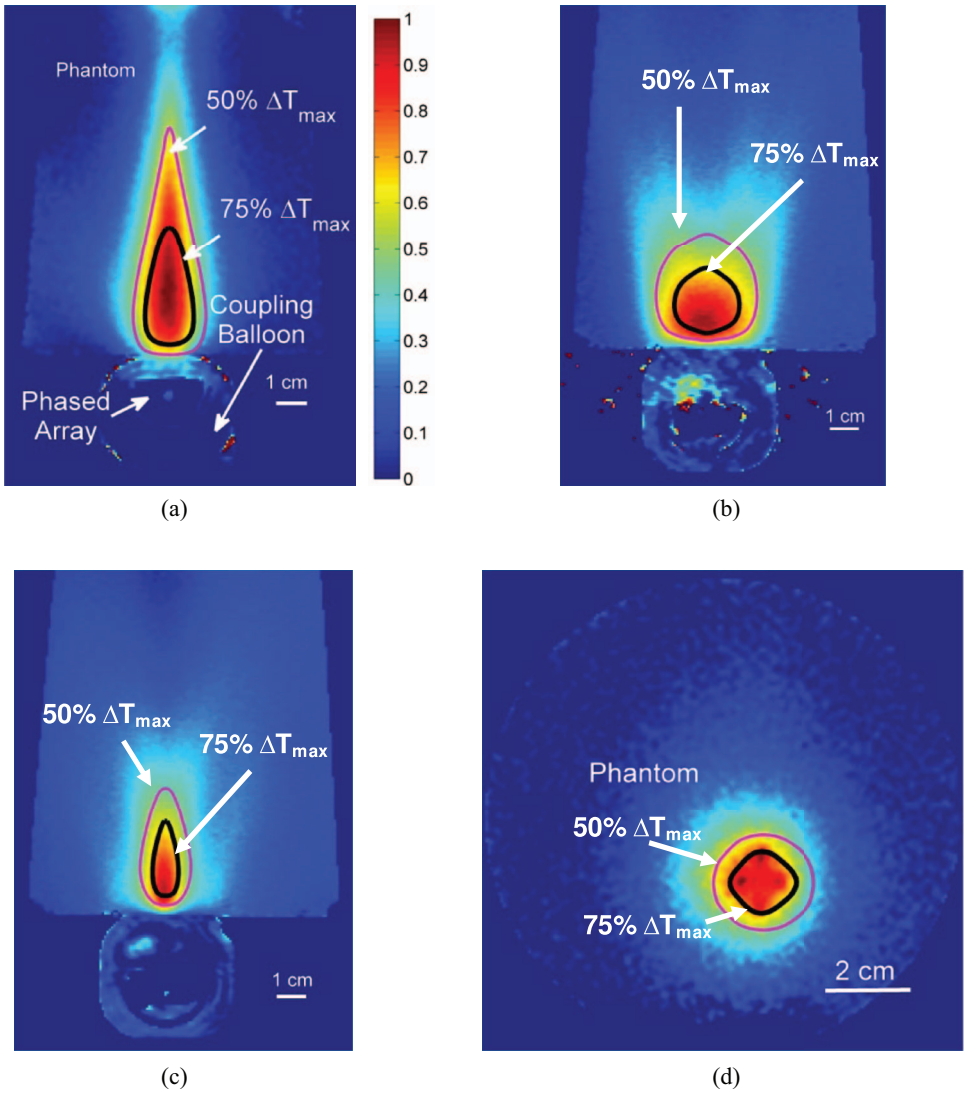

FIG. 8. MR temperature rise images captured during CW sonications in tissue mimicking phantoms with ExAblate 2100 prostate array are shown here (0.88 W/cm^2, 15 min.). Heating from (a) Iso-phase/planar, (b) diverging and (c) curvilinear in axial plane and (d) simultaneous multi-focused sonications in coronal plane are shown. Temperatures have been normalized to maximum temperature measured during sonication. Simulated contours of 50% and 75% maximum temperature have been overlaid.

water (22 °C) flow was maintained throughout the exposures (Fig. 8). Temperature profiles were also simulated for tissue mimicking phantom consistent with experiment parameters and physical properties of the phantom. Numerical simulations were based on transient generalized model discussed earlier. For hyperthermia treatments, maximum temperatures of 43–45 °C (6–8 °C temperature rise) are desired and temperature volumes of 41 °C (4 °C temperature) are of interest. Volumes where the temperature rise is 50% and 75% of the maximum value of temperature rise were compared between simulation and experiments.

3. RESULTS

3.A. Acoustic calculations

Acoustic fields for various focusing patterns were calculated to investigate simultaneous multipoint focusing and shaped energy deposition patterns for generating hyperthermia. The ExAblate ERUS array was designed for HIFU ablation by creating tight acoustic focal spots, especially along its axis. Calculated acoustic fields indicated a 3-dB beamwidth for focusing depths of 20–40 mm was 0.6–1.15 mm in the elevation dimension and 0.4–0.65 mm in the azimuth dimension. Off-axis focusing resulted in some energy deposition in the side lobes. The ratio of maximum acoustic intensity values in the side lobe and the main lobe was computed in the focusing plane and was used to quantify capability for off-axis focusing and beam steering. At a focusing depth of 20 mm and off-axis focusing position of 5–10 mm, maximum energy in the side lobe was 5%–20.0% of maximum energy in the main lobe. At a 30 mm depth, this proportion was 2.5%–15.5% and at 40 mm depth it was 1.4%–6.0%. Single-point focusing is more relevant to HIFU ablation. This analysis helped in ascertaining limits of off-axis focusing for complex beam forming or electronic scanning specifically developed for hyperthermia. Similar trends were observed when

TABLE II. Treatable volumes obtained by multipoint focusing in generalized models. The number of simultaneous focusing points was varied. Power input was adjusted to achieve maximum temperature close to 45 °C, within limits and constraints necessary for safe operation on ExAblate 2100. Constant blood perfusion of 2 kg/m^3/s was assumed.

Number	Is (W/cm^2)	T_{max} (°C)	V_{40} (cm^3)	V_{41} (cm^3)
4	0.68	45.2	8.8	4.5
6	0.7	45.1	9.6	5.2
8	0.72	45.1	10.6	5.8

curvilinear focusing was employed. When focused in the elevation dimension, focusing depths below 25 mm resulted in peak side-lobe intensity values in excess of 10% of peak intensity in the main lobe.

3.B. Generalized models

Therapeutic volumes V_{40} and V_{41} (volumes of isothermal clouds of 40 and 41 °C, respectively) were determined for different sonication/beamforming strategies and the results are presented in Tables II–V. A constant blood perfusion rate of 2 kg/m^3/s was assumed for these models. With simultaneous multipoint focusing V_{40} and V_{41} were small. For 4–8 focusing points, V_{40} was between 8.8 and 10.6 cm^3 and V_{41} was between 4.5 and 5.8 cm^3. With curvilinear focusing in elevation direction at depth of 25 and 35 mm along the propagation axis, $V_{40} = 12$ cm^3 and $V_{41} = 6$ cm^3, respectively, were calculated. Larger treatable volumes were calculated for diffused sonications. With diverging and planar patterns, $V_{40} = 24$ –35 cm^3 and $V_{41} = 12$–22 cm^3 were computed.

3.B.1. Parametric analysis

Results from a parametric study utilizing planar sonications are presented in Tables VI–VIII. Impact of blood perfusion variation on heating performance was studied by changing perfusion between 0.5 and 8.0 kg/m^3/s.[54] The input acoustic intensity was varied with perfusion between 0.61 and 2.15 W/cm^2. Dimensions of the 40 and 41 °C isotemperature contours were computed. In the azimuthal direction (along applicator width), dimensions of these contours varied from 33 to 26 mm and 27 to 22 mm, respectively, with increasing perfusion. In the elevation direction (along applicator length), variations in contour dimensions were lower, spanning 40 –37 mm and 35–33 mm. Depth of tissue heating for both contours were 71.5–69 mm and 67–59 mm. For these models, applicator cooling was held constant at 30 °C.

TABLE III. Treatable volumes obtained by cylindrical or curvilinear focusing in generalized models. The focal depth was varied. Power input was adjusted to achieve maximum temperature close to 45 °C, within limits and constraints necessary for safe operation on ExAblate 2100. Constant blood perfusion of 2 kg/m^3/s was assumed.

Depth (mm)	Is (W/cm^2)	T_{max} (°C)	V_{40} (cm^3)	V_{41} (cm^3)
25	0.75	45.1	12.1	6.0
35	0.7	44.9	12.7	6.6

TABLE IV. Treatable volumes obtained by divergent focusing in generalized models. Array beamforming was utilized to simulate cylindrical transducers with different radii of curvature and fixed aperture width of 2.3 cm (same as array width). Power input was adjusted to achieve maximum temperature close to 45 °C, within limits and constraints necessary for safe operation on ExAblate 2100. Constant blood perfusion of 2 kg/m^3/s was assumed.

Radius of curvature (mm)	Is (W/cm^2)	T_{max} (°C)	V_{40} (cm^3)	V_{41} (cm^3)
10	1.05	44.7	24.4	13.3
20	1.13	44.7	26.3	13.8
40	1.2	44.8	37.2	21.5

The impact of applicator cooling for long duration sonication with the ExAblate 2100 array was studied by varying T_{cool} between 22 and 35 °C for planar sonication configuration discussed above (Table VII). Perfusion was held constant at 2.0 kg/m^3/s. Across the range of T_{cool} values considered, slight changes in applied power ranging from 1.05 to 0.92 W/cm^2 were needed to maintain $T_{max} \sim 45$ °C. With changes in T_{cool}, dimensions of the 40 and 41 °C contours showed minimal changes (<2 mm) in azimuth or elevation dimensions. In the range dimension, reduced cooling caused some reduction in heating depth.

Hardware constraints imposed on the ExAblate 2100 system for applicator protection during long duration sonications may require shorter duty cycles instead of continuous sonication. Hence, transient models employing planar sonications were implemented to study the impact of duty cycle variation on heating performance. Duty cycle was varied between 80%, 88%, and 100% with pulse repetition frequencies of 0.0104 Hz, 0.011 Hz, and CW. The blood perfusion rate was set to 2.0 kg/m^3/s and T_{cool} was held constant at 30 °C. Peak acoustic intensity was varied such that the total energy delivered in a single pulse cycle was constant and the maximum temperature was close to 45 °C. After 12 min into the treatment, steady temperature levels were achieved with 100% duty cycles. After this time instance, the observed temperature ripple in T_{max} was below 0.1 and 0.3 °C for the 88% and 80% duty cycle cases, respectively. Similar small ripples were also seen in isotemperature volumes (Fig. 7). For this comparison, dimensions of volume contours for thermal doses of 6 and 10 CEM43 were also calculated. For 100%, 88%, and 80% duty cycles, the isodose cloud dimensions were within a millimeter agreement (Table VIII).

TABLE V. Treatable volumes obtained by planar or isophase focusing in generalized models. Power input was adjusted to achieve maximum temperature close to 45 °C, within limits and constraints necessary for safe operation on ExAblate 2100. Constant blood perfusion of 2 kg/m^3/s was assumed.

Type	Is (W/cm^2)	T_{max} (°C)	V_{40} (cm^3)	V_{41} (cm^3)
Planar	0.94	44.7	35	22.8

TABLE VI. Parametric study was conducted using planar sonication implemented in steady state generalized models to study the impact of perfusion on heat delivery. The perfusion was varied between 0.5 and 8.0 kg/m^3/s. Acoustic intensity was varied such that the maximum temperature was close to 45 °C. Dimensions of 40 and 41 °C contours are reported here. Azim refers to dimension along transducer width, Elev refers to the dimension along array length, Range refers to axial depth from transducer surface, and Spare refers to distance of tissue from cooling/coupling balloon which was thermally spared (not heated above 40 or 41 °C). Cooling around the device was held constant and the balloon was modeled as a constant temperature boundary at 30 °C.

			40 °C contour dimensions				41 °C contour dimensions			
ω_b (kg/m^3/s)	I (W/cm^2)	T_{max} (°C)	Azim (mm)	Elev (mm)	Range (mm)	Spare (mm)	Azim (mm)	Elev (mm)	Range (mm)	Spare (mm)
0.5	0.61	45.02	33	40	71.5	21.5	27	35	67	23
2.0	0.99	45.06	29	38	71	20	24	34	65	21
4.0	1.43	44.98	26	37	70	19	23	34	62.5	20
8.0	2.15	44.96	26	37	69	17.5	22	33	59	18.5

3.C. Patient-specific models

3.C.1. Multipoint focusing

An example of such multipoint focusing is shown in Fig. 3, where conformal hyperthermia to a small focal target in right posterior quadrant of the prostate was simulated (patient case 1). For this preliminary effort, focal point placement was ascertained through a manual iterative process to maximize target coverage. The ERUS array was simultaneously focused on 6 points at an axial depth of 35 mm [Fig. 3(a)]. Foci were placed in the transverse plane such that the resultant heating best conformed to the target region shape. In the example shown here, acoustic intensity was 0.75 W/cm^2 (electrical power ∼9 W) and maximum temperature was 44.6 °C.

3.C.2. Cylindrical or curvilinear focusing

The example shown in Fig. 4 shows curvilinear focusing employed to target the cancer site from patient case 1. In this case, the focusing axis was placed along the array azimuth and the focal depth was 35 mm from the array surface. This sonication pattern allowed heating in wedge-shaped patterns. The input was set to 0.7 W/cm^2 acoustic intensity (electrical power ∼8 W), which yielded a maximum temperature of 45 °C.

3.C.3. Planar sonications

Planar beam patterns were simulated by setting uniform phase values for all power channels. This achieved the effect of synchronous operation of all ERUS array elements to mimic the functionality of a planar rectangular transducer with a large aperture (Acoustic: 1.2 W/cm^2 or Electrical ∼14 W). As shown in Fig. 5, diffused energy deposition spread out over a larger volume was possible with this configuration. For this representative case, therapeutic hyperthermia could be delivered to targets in the posterior quadrant of the prostate could be treated, extending to the prostate boundary.

3.C.4. Diverging sonications

Diverging acoustic beam patterns were simulated to heat wide targets in posterior prostate (Fig. 6). Patient specific models were used to explore the possibility of heating bilateral targets with this configuration. The representative case shown in Fig. 6 contains a target primarily in the left posterior quadrant with a section extending past the urethra into the right quadrant. To heat this target, beamforming was used to simulate a cylindrical transducer with a 60-mm radius of curvature and 2.3 cm wide aperture. This resulted in wave fronts similar to tubular transducer elements (cylindrically diverging or defocused). As compared to the planar sonication strategy, angular expanse of energy deposition across the array azimuth was increased. However, higher input power (Acoustic:

TABLE VII. Parametric study was conducted using planar sonication implemented in steady state generalized models to study the impact of applicator cooling on heat delivery. Cooling was varied from 22 to 35 °C. The perfusion was set to 2.0 kg/m^3/s. Acoustic intensity was varied such that the maximum temperature was close to 45 °C. Dimensions of 40 and 41 °C contours are reported here. Azim, Elev, Range, and Spare are same as in previous table.

			40 °C contour dimensions				41 °C contour dimensions			
T_c (°C)	I (W/cm^2)	T_{max} (°C)	Azim (mm)	Elev (mm)	Range (mm)	Spare (mm)	Azim (mm)	Elev (mm)	Range (mm)	Spare (mm)
22	1.05	45.01	28	38	71.5	22.5	24	34	66.5	23.5
30	0.99	45.06	29	38	71	20	24	34	65	21
35	0.92	44.94	28	38	69.5	17.5	24	34	63	19

TABLE VIII. Parametric study was conducted using planar sonication implemented in transient generalized models to study the impact of sonication duty cycle on heat delivery. Duty cycle was varied between 80%, 88%, and 100% with pulse repetition frequency 0.0104, 0.011 Hz and CW. The perfusion was set to 2.0 kg/m^3/s and cooling temperature was held constant at 30 °C. Peak acoustic intensity was varied such that the total energy delivered in a single pulse cycle was constant and the maximum temperature was close to 45 °C. Dimensions of $t_{43} > 6$ min and $t_{43} > 10$ min contours are reported here. Azim, Elev, Range, and Spare are same as in previous tables.

			$t_{43} > 6$ min contour dimensions				$t_{43} > 10$ min contour dimensions			
Duty cycle (%)	I (W/cm^2)	T_{max} (°C)	Azim (mm)	Elev (mm)	Range (mm)	Spare (mm)	Azim (mm)	Elev (mm)	Range (mm)	Spare (mm)
100	0.99	45.06	20	32	56	23	18.8	28	53	23
88	1.12	45.06	20	32	56	23	18	28	53	23
80	1.25	45.28	20	32	56	23	18	28	53	23

1.35 W/cm^2, Electrical ~16 W) was required to achieve therapeutic temperatures. Also, energy deposition in the side lobes was more difficult to control.

3.D. Evaluation in tissue phantom under MRTI

Based on the proprietary irregular transducer element layout and wiring scheme of the ExAblate 2100 array, phasing patterns were calculated to generate the following sonication patterns and applied within phantom to evaluate generated temperature distributions (Fig. 8).

- Planar sonication was performed using isophase/synchronous excitation of the transducer array elements. This was similar to placing a single focal point at a very large distance from the array and resulted in heating volumes close to the array determined by the width of the array.
- Diverging pattern was created by placing the synthetic focus 40 mm behind the array, on its axis and along array elevation dimension. This caused heating in a cylindrically defused volume with its extent greater than the array width.
- Curvilinear pattern with synthetic focus at 40 mm distance on the array axis, and along array elevation dimension. This resulted in wedge shaped heating volumes caused by cylindrical focusing.
- Simultaneous multipoint focusing was demonstrated using four-point focusing pattern where the foci were placed at 35 mm distance from the array at a distance of 5 mm from the central axis of the array. This resulted in a "plus"-shaped heating pattern evident in temperature distribution seen in the coronal plane.

Phase delays associated with these beamformed sonications were programmed into the ExAblate system using the control computer interface. Figure 8 depicts temperature profiles in tissue mimicking phantoms temperature rise after prolonged heating with a relatively low intensity setting of 0.88 W/cm^2 (acoustic). Temperature rises were obtained by reconstructing MR images (PRFS). The images have been normalized to maximum temperature values, which were 22.5 °C for planar, 11.2 °C for cylindrically diverging, 16.7 °C for curvilinear focused, and 20.6 °C for multipoint focused beam patterns. Contours of 50% and 75% maximum temperature estimated by numerical models of phantom heating have been overlaid. A general agreement can be observed between shapes of heated regions based on experiment and simulation. Experiments and simulations for planar waveforms yielded 75% contour volumes of 6.4 and 6.5 cm^3, respectively, and 50% contour volumes of 22.5 and 19.4 cm^3, respectively. Experiments and simulations for cylindrically divergent beams yielded 75% contour volumes of 4.5 and 5.2 cm^3, respectively, and 50% contour volumes of 17.9 and 19.8 cm^3, respectively. Experiments and simulations for curvilinear focusing yielded 75% contour volumes of 1.3 and 2.1 cm^3, respectively, and 50% contour volumes were 7.1 and 8.9 cm^3, respectively. Experiments and simulations for multipoint focusing yielded 75% contour volumes of 2.3 and 1.8 cm^3, respectively, and 50% contour volumes of 8.9 and 7.2 cm^3, respectively.

4. DISCUSSION

The goal of this preliminary investigation was to evaluate feasibility of adapting the ExAblate 2100 ERUS ablation array within its hardware, software and operational constraints for delivering protracted mild hyperthermia to contiguous volumes in the prostate. This was examined through simulations and preliminary experiments. The generalized models were only designed to bracket potential treatment volumes for a range of physiological parameters including moderate to high perfusion levels, cooling levels and sonication switching times, all while adhering to power and hardware constraints of the ExAblate system. Tissue heterogeneity was considered in patient-specific models where representative cases were explored hyperthermia feasibility with ExAblate array for realistic prostate targets and anatomical geometry. Array beamforming can be utilized effectively to tailor energy deposition based upon the size and location of target volumes. Appropriate phasing patterns can enable targeting specific volumes in the posterior region of the gland, posterior quadrant hyperthermia and hemigland hyperthermia. Simultaneous multipoint focusing and curvilinear focusing can be employed to heat small targets (1.5–6.6 cm^3). With these sonications, energy can be delivered selectively with tailoring along the array length and in axial distance. Wide targets in

the posterior prostate can be effectively heated using divergent/diffuse sonications. These along with planar sonications may be effective in delivering quadrant or hemigland hyperthermia to large contiguous volumes (13.3–22.8 cm^3).

Initial experiments in tissue mimicking phantoms demonstrated the feasibility of implementing hyperthermia-specific array beamforming on the ExAblate array and delivery of protracted continuous wave sonications to generate hyperthermia in contiguous volumes under MRTI. A general agreement was observed between theoretical simulations and experiments with consistency between overall shapes of energy deposition and phantom heating. Differences may be partly attributed to using approximate values for the acoustic and thermal properties of the phantom, and approximations to coupling of convective cooling. Further, the small differences between measured and simulated temperature values may in part be attributed to non piston-like vibration behavior of the phased array elements.[55] Observed differences in simulated and measured temperatures can be resolved in practice through accurate power calibration and implementation of feedback control with MRTI during implementation.

A single-channel brain coil was used for MR imaging during these experiments. This choice was made to simplify the experimental set up. In clinical practice, a multichannel pelvic coil, which can be wrapped around the patient with a belt strap, will be used. Pelvic and brain coil have similar SNR levels for proton resonance frequency shift sequences used during MR thermometry. The feasibility of long term MR thermometry during pelvic hyperthermia has been demonstrated using proton resonance frequency shift (PRFS) imaging methods utilized here. Temperature measurements with accuracy of 0.3–1 °C have been reported.[56–60] In addition to the standard PRFS techniques utilized here, it may be possible to improve SNR using drift correction techniques and longer echo times.

ExAblate 2100 has approval for clinical trials pertaining to prostate ablation.[41–43] Potentially, it can be fast tracked into the clinic for hyperthermia applications as well. Feasibility of safe hyperthermia delivery to the prostate using transrectal ultrasound arrays (∼1.5 MHz, 4–16 elements) has been reported in the past.[28–30] Diverging sonications with ExAblate array can be used to deliver diffuse hyperthermia similar to cylindrical-element applicators described in the aforementioned studies. Greater control of heating may be possible due to greater array beamforming possibilities arising from larger number of elements, mechanical rotation and translation capabilities, and volumetric thermal dosimetry through MR temperature monitoring. This may enable precise energy delivery to the prostate while limiting thermal dose to critical structures such as urethra, neurovascular bundles, and pubic bones.

Some recent studies have reported hyperthermia delivery to small tissue volumes using commercial MR-guided extracorporeal HIFU ablation applicators. These studies consisted of animal experiments designed to study enhanced delivery and uptake of drugs using sub-lethal thermal doses. In Refs. 35–37, extracorporeal phased array included in ExAblate 2000 by InSightec was employed for pulsed-HIFU sonications in small (∼45 mm^3) implanted murine tumors under MR-guidance with the goal to cause mild temperature increases. These sonications were only limited to sequential focusing at multiple points, available as part of ablation tools within the ExAblate system. Short duty cycles were employed to limit temperature rises. CW sonications which employ electronic and mechanical scanning of a single HIFU focus under MR-guidance have also been explored to deliver hyperthermia with another commercial ablation system (Sonalleve, Philips Medical Systems, Vantaa, Finland). The animal study in Ref. 39 demonstrates treatment of small volumes (treatment cell diameter of 4–16 mm) with fast translation of the HIFU focus. In another study by the same group, multipoint focusing was implemented on the same HIFU system to treat target volumes with ∼15 mm diameter.[34]

The prostate array from ExAblate 2100 system is designed for endocavity placement as opposed to the external arrays employed in the aforementioned studies, and hence has stringent size and design constraints. Hyperthermia delivery to large treatment volumes with this small array requires more meticulous planning, but it can also offer therapeutic advantages. Targeted CW sonications to treat large and deep cancer targets are more feasible with an endocavity array because it is less susceptible to organ motion and intervening tissue structures as compared to an external applicator. Effective heating of larger volumes opens the possibility of heating hemigland prostate or bilateral targets. Simultaneous multifocus beamforming can also be implemented on InSightec prostate array to conformably heat smaller targets, and it can potentially produce more steady temperature profiles than electronic scanning of HIFU focus.

Array design constraints on the ExAblate 2100 prostate array such as element layout and element connections place limits on electronic scanning, focal gains, and side-lobe generation when compared to ERUS arrays considered for hyperthermia during earlier studies.[21–30] Whole gland hyperthermia may not be possible simply through beamforming alone. However, the ExAblate 2100 has a rotational and translational positioning module that affords accurate positioning and orientation of the applicator within the patient. Hence, lateral regions of the gland can be treated sequentially to effectively produce whole gland heating. Further, it may be possible to apply frequent and rapid mechanical translation/rotation of the applicator to combine electronic and mechanical scanning. However motion-associated artifacts in MR thermometry could be problematic and may require MR-thermometry techniques which employ multiple baseline images for reliable temperature measurements in such scenarios.[61,62]

The relatively small size and low operating frequency of the array also limits targeting capability. The array can be used more effectively to target cancer in the posterior periphery of the gland; however, focal gain is reduced when targeting volumes placed toward the anterior border (for depths of greater than 45 mm). The low frequency can also result in energy deposition anterior to the prostate gland, especially during hemigland heating. This may result in heat generation in the pubic bone, especially in cases where it is close (within 5–10 mm) to the prostate. As seen in the representative

patient case 2 (Fig. 6), where the pubic bone is less than 1 cm from the gland, undesired heating can occur in the bone. Urethral cooling may also be necessary when heating hemigland or quadrant volumes. The patient cases shown here have cancer targets at the posterior periphery of the prostate close to the rectal wall. Cooling flow which protects the device and the rectum has to be carefully applied as excessive cooling can negatively impact hyperthermia delivery. As seen in Table VI, high input powers are required to induce therapeutic heating in large contiguous volumes when perfusion rate is high. However this also leads to larger power deposition near the array as seen by the reduction in "spared" tissue distance. In a clinical scenario when treating volumes with high perfusion, it may be necessary to increase rectal cooling to minimize rectal toxicity during sonications at high input powers. Hence it is imperative that clinical hyperthermia treatments should be carefully planned taking these sometimes counterintuitive factors and relations into consideration.

It should be noted that prostate cancer does not lead to distinct solid tumors and the cancer regions can be have heterogeneous physical properties and blood flow. The models developed in this study do not take into account such heterogeneity and dynamic changes in physiological parameters which can impact quality of a hyperthermia treatment. Treatment planning and optimization platforms will have to include such factors. Such accurate treatment modeling will be very complex. It is beyond the scope of this initial feasibility study. In clinical practice, MR-based temperature measurements may be utilized for real-time guidance of the therapy. It will be a useful tool in implementing temperature-based feedback control schemes where sonication phasing patterns (type of beamforming, number of focus points and placement of foci) and acoustic output from the ExAblate array may be changed dynamically to counter tumor heterogeneity and ensure safe and uniform hyperthermia to the target.

The ExAblate prostate array following operational modifications can be potentially used to exploit new treatment paradigms where hyperthermia may be combined with hypofractionated SBRT high dose rate radiation treatments.[30,63] It may be also be used in conjunction with temperature sensitive liposomes for targeted delivery of anti-cancer drugs to focal tumors.[19,39] Such transrectal hyperthermia delivery may be effective as part of multimodality regimens which incorporate chemotherapy and immunotherapy[64,65] to treat advanced or salvage cases of prostate cancer. Transurethral[66] or transrectal[67] hyperthermia has also been employed for treating chronic prostatitis, and similar treatments may be possible with the InSightec prostate array. The ExAblate prostate array may be potentially extended to hyperthermia treatments of other tumor sites in the pelvic cavity, such as rectum and anal canal. Future investigations that would be useful for implementing hyperthermia with this system could include the development of inverse planning algorithms to optimize beamforming schemes (such as multifocal patterns) specific for phased array prostate hyperthermia.[47,68,69] Temperature-based feedback control methods could possibly be implemented to improve target heating and avail the full power of MRTI for full 3D volumetric temperature feedback.

5. CONCLUSIONS

Simulations and preliminary experiments demonstrate the feasibility of delivering protracted mild hyperthermia 40–45 °C for >15–30 min to the prostate with ExAblate 2100 ERUS prostate ablation system. Phased array beamforming techniques may be used to tailor acoustic energy deposition pattern in 3D, along array length and angular expanse. Hyperthermia-specific beamforming strategies were implemented on the ExAblate system and continuous wave sonications generated therapeutic temperature rises during phantom experiments. Within hardware and software constraints imposed by the ERUS array design, it may be possible to administer protracted hyperthermia to posterior quadrants or hemigland prostate.

ACKNOWLEDGMENTS

This study was supported by grants from Focused Ultrasound (FUS) Foundation (Charlottesville, VA) and National Institutes of Health (NIH) (Grant Nos. R01CA122276 and R01CA111981).

[a]Electronic mail: salgaonkarv@radonc.ucsf.edu; Telephone: +1-415-353-9852.

[1]P. Wust, B. Hildebrandt, G. Sreenivasa, B. Rau, J. Gellermann, H. Riess, R. Felix, and P. Schlag, "Hyperthermia in combined treatment of cancer," Lancet Oncol. **3**, 487–497 (2002).
[2]J. Van der Zee, "Heating the patient: A promising approach?," Ann. Oncol. **13**, 1173–1184 (2002).
[3]E. L. Jones, J. R. Oleson, L. R. Prosnitz, T. V. Samulski, Z. Vujaskovic, D. Yu, L. L. Sanders, and M. W. Dewhirst, "Randomized trial of hyperthermia and radiation for superficial tumors," J. Clin. Oncol. **23**, 3079–3085 (2005).
[4]Z. Vujaskovic, D. W. Kim, E. Jones, L. Lan, L. Mccall, M. W. Dewhirst, O. Craciunescu, P. Stauffer, V. Liotcheva, and A. Betof, "A phase I/II study of neoadjuvant liposomal doxorubicin, paclitaxel, and hyperthermia in locally advanced breast cancer," Int. J. Hyperthermia **26**, 514–521 (2010).
[5]T. M. Zagar, J. R. Oleson, Z. Vujaskovic, M. W. Dewhirst, O. I. Craciunescu, K. L. Blackwell, L. R. Prosnitz, and E. L. Jones, "Hyperthermia combined with radiation therapy for superficial breast cancer and chest wall recurrence: A review of the randomised data," Int. J. Hyperthermia **26**, 612–617 (2010).
[6]R. D. Issels, L. H. Lindner, J. Verweij, P. Wust, P. Reichardt, B.-C. Schem, S. Abdel-Rahman, S. Daugaard, C. Salat, and C.-M. Wendtner, "Neo-adjuvant chemotherapy alone or with regional hyperthermia for localised high-risk soft-tissue sarcoma: A randomised phase 3 multicentre study," Lancet Oncol. **11**, 561–570 (2010).
[7]B. Hildebrandt, P. Wust, O. Ahlers, A. Dieing, G. Sreenivasa, T. Kerner, R. Felix, and H. Riess, "The cellular and molecular basis of hyperthermia," Crit. Rev. Oncol./Hematol. **43**, 33–56 (2002).
[8]A. M. Ponce, Z. Vujaskovic, F. Yuan, D. Needham, and M. W. Dewhirst, "Hyperthermia mediated liposomal drug delivery," Int. J. Hyperthermia **22**, 205–213 (2006).
[9]F. Lohr, K. Hu, Q. Huang, L. Zhang, T. V. Samulski, M. W. Dewhirst, and C.-Y. Li, "Enhancement of radiotherapy by hyperthermia-regulated gene therapy," Int. J. Radiat. Oncol., Biol., Phys. **48**, 1513–1518 (2000).
[10]J. Lagendijk, "Hyperthermia treatment planning," Phys. Med. Biol. **45**, R61–R76 (2000).

[11]T. P. Ryan, "Comparison of six microwave antennas for hyperthermia treatment of cancer: SAR results for single antennas and arrays," Int. J. Radiat. Oncol., Biol., Phys. **21**, 403–413 (1991).
[12]C. J. Diederich and K. Hynynen, "Ultrasound technology for hyperthermia," Ultrasound Med. Biol. **25**, 871–887 (1999).
[13]M. Seegenschmiedt, L. Brady, and R. Sauer, "Interstitial thermoradiotherapy: Review on technical and clinical aspects," Am. J. Clin. Oncol. **13**, 352–363 (1990).
[14]J. H. Wootton, P. Prakash, I. C. J. Hsu, and C. J. Diederich, "Implant strategies for endocervical and interstitial ultrasound hyperthermia adjunct to HDR brachytherapy for the treatment of cervical cancer," Phys. Med. Biol. **56**, 3967–3984 (2011).
[15]J. Crezee, P. Van Haaren, H. Westendorp, M. De Greef, H. Kok, J. Wiersma, G. Van Stam, J. Sijbrands, P. Zum Varde Sive Varding, and J. Van Dijk, "Improving locoregional hyperthermia delivery using the 3-D controlled AMC-8 phased array hyperthermia system: A preclinical study," Int. J. Hyperthermia **25**, 581–592 (2009).
[16]K. A. Leopold, M. W. Dewhirst, T. V. Samulski, R. K. Dodge, S. L. George, J. L. Blivin, L. R. Prosnitz, and J. R. Oleson, "Cumulative minutes with T_{90} greater than $temp_{index}$ is predictive of response of superficial malignancies to hyperthermia and radiation," Int. J. Radiat. Oncol., Biol., Phys. **25**, 841–847 (1993).
[17]M. Franckena, D. Fatehi, M. Bruijne, R. A. M. Canters, Y. Norden, J. W. Mens, G. C. Rhoon, and J. Zee, "Hyperthermia dose-effect relationship in 420 patients with cervical cancer treated with combined radiotherapy and hyperthermia," Eur. J. Cancer **45**, 1969–1978 (2009).
[18]C. J. Diederich, J. Wootton, P. Prakash, V. Salgaonkar, T. Juang, S. Scott, X. Chen, A. Cunha, J. Pouliot, and I. Hsu, "Catheter-based ultrasound hyperthermia with HDR brachytherapy for treatment of locally advanced cancer of the prostate and cervix," *Proceedings of SPIE* (Energy-based Treatment of Tissue and Assessment VI, Vol. 7901, 2011), pp. 79010–79018.
[19]D. Needham and M. W. Dewhirst, "The development and testing of a new temperature-sensitive drug delivery system for the treatment of solid tumors," Adv. Drug Delivery Rev. **53**, 285–305 (2001).
[20]P. Wust, C. H. Cho, B. Hildebrandt, and J. Gellermann, "Thermal monitoring: Invasive, minimal-invasive and non-invasive approaches," Int. J. Hyperthermia **22**, 255–262 (2006).
[21]C. J. Diederich and K. Hynynen, "The development of intracavitary ultrasonic applicators for hyperthermia: A design and experimental study," Med. Phys. **17**, 626–634 (1990).
[22]C. Diederich and K. Hynynen, "The feasibility of using electrically focused ultrasound arrays to induce deep hyperthermia via body cavities," IEEE Trans. Ultrason. Ferroelectr. Freq. Control **38**, 207–219 (1991).
[23]M. T. Buchanan and K. Hynynen, "Design and experimental evaluation of an intracavitary ultrasound phased array system for hyperthermia," IEEE Trans. Biomed. Eng. **41**, 1178–1187 (1994).
[24]L. Gavrilov and J. Hand, "Development and investigation of ultrasound linear phased arrays for transrectal treatment of prostate," Ultrason. Sonochem. **4**, 173–174 (1997).
[25]E. Hutchinson, M. Dahleh, and K. Hynynen, "The feasibility of MRI feedback control for intracavitary phased array hyperthermia treatments," Int. J. Hyperthermia **14**, 39–56 (1998).
[26]N. B. Smith, M. T. Buchanan, and K. Hynynen, "Transrectal ultrasound applicator for prostate heating monitored using MRI thermometry," Int. J. Radiat. Oncol., Biol., Phys. **43**, 217–225 (1999).
[27]M. Hurwitz, I. Kaplan, G. Svensson, M. Hansen, and K. Hynynen, "Feasibility and patient tolerance of a novel transrectal ultrasound hyperthermia system for treatment of prostate cancer," Int. J. Hyperthermia **17**, 31–37 (2001).
[28]H. Fosmire, K. Hynynen, G. W. Drach, B. Stea, P. Swift, and J. R. Cassady, "Feasibility and toxicity of transrectal ultrasound hyperthermia in the treatment of locally advanced adenocarcinoma of the prostate," Int. J. Radiat. Oncol., Biol., Phys. **26**, 253–259 (1993).
[29]M. D. Hurwitz, I. D. Kaplan, J. L. Hansen, S. Prokopios-Davos, G. P. Topulos, K. Wishnow, J. Manola, B. A. Bornstein, and K. Hynynen, "Hyperthermia combined with radiation in treatment of locally advanced prostate cancer is associated with a favourable toxicity profile," Int. J. Hyperthermia **21**, 649–656 (2005).
[30]M. D. Hurwitz, J. L. Hansen, S. Prokopios-Davos, J. Manola, Q. Wang, B. A. Bornstein, K. Hynynen, and I. D. Kaplan, "Hyperthermia combined with radiation for the treatment of locally advanced prostate cancer," Cancer **117**, 510–516 (2011).
[31]F. A. Jolesz, K. Hynynen, N. McDannold, and C. Tempany, "MR imaging-controlled focused ultrasound ablation: A noninvasive image-guided surgery," Magn. Reson. Imaging Clin. North Am. **13**, 545–560 (2005).
[32]C. M. Tempany, N. J. McDannold, K. Hynynen, and F. A. Jolesz, "Focused ultrasound surgery in oncology: Overview and principles," Radiology **259**, 39–56 (2011).
[33]F. A. Jolesz, "MRI-guided focused ultrasound surgery," Annu. Rev. Med. **60**, 417–430 (2009).
[34]A. Partanen, M. Tillander, P. S. Yarmolenko, B. J. Wood, M. R. Dreher, and M. O. Kahler, "Reduction of peak acoustic pressure and shaping of heated region by use of multifoci sonications in MR-guided high-intensity focused ultrasound mediated mild hyperthermia," Med. Phys. **40**, 013301 (13pp.) (2013).
[35]Z. Mu, C. Ma, X. Chen, D. Cvetkovic, A. Pollack, and L. Chen, "MR-guided pulsed high intensity focused ultrasound enhancement of docetaxel combined with radiotherapy for prostate cancer treatment," Phys. Med. Biol. **57**, 535–545 (2012).
[36]L. Chen, Z. Mu, P. Hachem, C. Ma, A. Wallentine, and A. Pollack, "MR-guided focused ultrasound: Enhancement of intratumoral uptake of [3H]-docetaxel in vivo," Phys. Med. Biol. **55**, 7399–7741 (2010).
[37]X. Chen, D. Cvetkovic, C.-M. Ma, and L. Chen, "Quantitative study of focused ultrasound enhanced doxorubicin delivery to prostate tumor in vivo with MRI guidance," Med. Phys. **39**, 2780–2786 (2012).
[38]R. Staruch, R. Chopra, and K. Hynynen, "Localised drug release using MRI-controlled focused ultrasound hyperthermia," Int. J. Hyperthermia **27**, 156–171 (2011).
[39]A. Partanen, P. S. Yarmolenko, A. Viitala, S. Appanaboyina, D. Haemmerich, A. Ranjan, G. Jacobs, D. Woods, J. Enholm, and B. J. Wood, "Mild hyperthermia with magnetic resonance-guided high-intensity focused ultrasound for applications in drug delivery," Int. J. Hyperthermia **28**, 320–336 (2012).
[40]R. Staruch, R. Chopra, and K. Hynynen, "Hyperthermia in bone generated with MR imaging controlled focused ultrasound: Control strategies and drug delivery," Radiology **263**, 117–127 (2012).
[41]A. Napoli, M. Anzidei, C. De Nunzio, G. Cartocci, V. Panebianco, C. De Dominicis, C. Catalano, F. Petrucci, and C. Leonardo, "Real-time magnetic resonance guided high-intensity focused ultrasound focal therapy for localised prostate cancer: Preliminary experience," Eur. Urol. **63**, 395–398 (2012).
[42]U. Lindner, S. Ghai, P. Spensieri, E. Hlasny, T. H. Van der Kwast, S. A. McCluskey, M. A. Haider, W. Kucharczyk, and J. Trachtenberg, "Focal magnetic resonance guided focused ultrasound for prostate cancer: Initial North American experience," Can. Urol. Assoc. J. **6**, E283–E286 (2012).
[43]FUSFoundation, "InSightec provides update on its prostate cancer clinical trial," (available URL: http://www.fusfoundation.org/news/129-press-room/500-mens-health-update-from-fus-foundation-spotlights-new-minimally-invasive-treatments-for-prostate-cancer-and-bph-sp-702?highlight=WyJjbGluaWNhbCIsInRyaWFscyIsImNsaW5pY2FsIHRyaWFscyJd).
[44]K. B. Ocheltree and L. Frizzel, "Sound field calculation for rectangular sources," IEEE Trans. Ultrason. Ferroelectr. Freq. Control **36**, 242–248 (1989).
[45]J. H. Wootton, A. B. Ross, and C. J. Diederich, "Prostate thermal therapy with high intensity transurethral ultrasound: The impact of pelvic bone heating on treatment delivery," Int. J. Hyperthermia **23**, 609–622 (2007).
[46]K. Saleh and N. Smith, "Two-dimensional ultrasound phased array design for tissue ablation for treatment of benign prostatic hyperplasia," Int. J. Hyperthermia **20**, 7–31 (2004).
[47]R. J. McGough, E. S. Ebbini, and C. A. Cain, "Direct computation of ultrasound phased-array driving signals from a specified temperature distribution for hyperthermia," IEEE Trans. Biomed. Eng. **39**, 825–835 (1992).
[48]A. H. Aitkenhead, J. A. Mills, and A. J. Wilson, "The design and characterization of an ultrasound phased array suitable for deep tissue hyperthermia," Ultrasound Med. Biol. **34**, 1793–1807 (2008).
[49]H. H. Pennes, "Analysis of tissue and arterial blood temperatures in the resting human forearm," J. Appl. Physiol. **1**, 93–122 (1948).
[50]G. Raaphorst, D. Heller, A. Bussey, and C. Ng, "Thermal radiosensitization by 41 C hyperthermia during low dose-rate irradiation in human normal and tumour cell lines," Int. J. Hyperthermia **10**, 263–270 (1994).
[51]M. W. Dewhirst, Z. Vujaskovic, E. Jones, and D. Thrall, "Re-setting the biologic rationale for thermal therapy," Int. J. Hyperthermia **21**, 779–790 (2005).

[52]B. O'Neill, C. Karmonik, and K. Li, "An optimum method for pulsed high intensity focused ultrasound treatment of large volumes using the InSightec ExAblate® 2000 system," Phys. Med. Biol. **55**, 6395–6410 (2010).
[53]V. Rieke and K. Butts Pauly, "MR thermometry," J. Magn. Reson. Imaging **27**, 376–390 (2008).
[54]B. Raaymakers, M. Van Vulpen, J. Lagendijk, A. De Leeuw, J. Crezee, and J. Battermann, "Determination and validation of the actual 3D temperature distribution during interstitial hyperthermia of prostate carcinoma," Phys. Med. Biol. **46**, 3115–3131 (2001).
[55]A. H. Aitkenhead, J. A. Mills, and A. J. Wilson, "An analysis of the origin of differences between measured and simulated fields produced by a 15-element ultrasound phased array," Ultrasound Med. Biol. **36**, 410–418 (2010).
[56]J. Gellermann, W. Wlodarczyk, A. Feussner, H. Fähling, J. Nadobny, B. Hildebrandt, R. Felix, and P. Wust, "Methods and potentials of magnetic resonance imaging for monitoring radiofrequency hyperthermia in a hybrid system," Int. J. Hyperthermia **21**, 497–513 (2005).
[57]J. Gellermann, W. Wlodarczyk, H. Ganter, J. Nadobny, H. Fähling, M. Seebass, R. Felix, and P. Wust, "A practical approach to thermography in a hyperthermia/magnetic resonance hybrid system: Validation in a heterogeneous phantom," Int. J. Radiat. Oncol., Biol., Phys. **61**, 267–277 (2005).
[58]M. Weihrauch, P. Wust, M. Weiser, J. Nadobny, S. Eisenhardt, V. Budach, and J. Gellermann, "Adaptation of antenna profiles for control of MR guided hyperthermia (HT) in a hybrid MR-HT system," Med. Phys. **34**, 4717–4725 (2007).
[59]O. I. Craciunescu, P. R. Stauffer, B. J. Soher, C. R. Wyatt, O. Arabe, P. Maccarini, S. K. Das, K.-S. Cheng, T. Z. Wong, and E. L. Jones, "Accuracy of real time noninvasive temperature measurements using magnetic resonance thermal imaging in patients treated for high grade extremity soft tissue sarcomas," Med. Phys. **36**, 4848–4858 (2009).
[60]P. R. Stauffer, O. I. Craciunescu, P. F. Maccarini, C. R. Wyatt, K. Arunachalam, O. Arabe, V. Stakhursky, B. Soher, J. R. MacFall, Z. Li, W. T. Joines, S. Rangarao, K. S. Cheng, S. K. Das, C. D. Martins, C. Charles, M. W. Dewhirst, T. Wong, E. Jones, and Z. Vujaskovic, "Clinical Utility of Magnetic Resonance Thermal Imaging (MRTI) For Realtime Guidance of Deep Hyperthermia," *Proceedings of SPIE* (Energy-based Treatment of Tissue and Assessment V, Vol. 7181, 2009), pp. 71810I-1–71810I-12.
[61]B. D. de Senneville, S. b. Roujol, C. Moonen, and M. Ries, "Motion correction in MR thermometry of abdominal organs: A comparison of the referenceless vs. the multibaseline approach," Magn. Reson. Med. **64**, 1373–1381 (2010).
[62]B. Quesson, C. Laurent, G. Maclair, B. D. de Senneville, C. Mougenot, M. Ries, T. Carteret, A. Rullier, and C. T. Moonen, "Real-time volumetric MRI thermometry of focused ultrasound ablation in vivo: A feasibility study in pig liver and kidney," NMR Biomed. **24**, 145–153 (2011).
[63]M. D. Hurwitz, "Today's thermal therapy: Not your father's hyperthermia: Challenges and opportunities in application of hyperthermia for the 21st century cancer patient," Am. J. Clin. Oncol. **33**, 96–100 (2010).
[64]B. Stawarz, H. Zielinski, S. Szmigielski, E. Rappaport, P. Debicki, and Z. Petrovich, "Transrectal hyperthermia as palliative treatment for advanced adenocarcinoma of prostate and studies of cell-mediated immunity," Urology **41**, 548–553 (1993).
[65]B. Frey, E.-M. Weiss, Y. Rubner, R. Wunderlich, O. J. Ott, R. Sauer, R. Fietkau, and U. S. Gaipl, "Old and new facts about hyperthermia-induced modulations of the immune system," Int. J. Hyperthermia **28**, 528–542 (2012).
[66]N. G. Choi, S. H. Soh, T. H. Yoon, and M. H. Song, "Clinical experience with transurethral microwave thermotherapy for chronic nonbacterial prostatitis and prostatodynia," J. Endourol. **8**, 61–64 (1994).
[67]M. Gao, H. Ding, G. Zhong, J. Lu, H. Wang, Q. Li, and Z. Wang, "The effects of transrectal radiofrequency hyperthermia on patients with chronic prostatitis and the changes of MDA, NO, SOD, and Zn levels in pretreatment and posttreatment," Urology **79**, 391–396 (2012).
[68]E. S. Ebbini and C. A. Cain, "Multiple-focus ultrasound phased-array pattern synthesis: Optimal driving-signal distributions for hyperthermia," IEEE Trans. Ultrason. Ferroelectr. Freq. Control **36**, 540–548 (1989).
[69]D. Daum and K. Hynynen, "Theoretical design of a spherically sectioned phased array for ultrasound surgery of the liver," Eur. J. Ultrasound **9**, 61–69 (1999).
[70]S. Goss, R. Johnston, and F. Dunn, "Comprehensive compilation of empirical ultrasonic properties of mammalian tissues," J. Acoust. Soc. Am. **64**, 423–457 (1978).
[71]K. Hynynen and D. DeYoung, "Temperature elevation at muscle-bone interface during scanned, focused ultrasound hyperthermia," Int. J. Hyperthermia **4**, 267–279 (1988).